Journal of Alzheimer's Disease 55 (2017) 1537–1548
DOI 10.3233/JAD-160760
IOS Press

Longitudinal Characterization of [^{18}F]-FDG and [^{18}F]-AV45 Uptake in the Double Transgenic TASTPM Mouse Model

Ann-Marie Waldron[a], Leonie wyffels[a,b], Jeroen Verhaeghe[a], Jill C. Richardson[c], Mark Schmidt[d], Sigrid Stroobants[a,b], Xavier Langlois[d] and Steven Staelens[a,*]
[a]*Molecular Imaging Center Antwerp, University of Antwerp, Antwerp, Belgium*
[b]*Department of Nuclear Medicine, University Hospital Antwerp, Antwerp, Belgium*
[c]*R&D China U.K. Group, GlaxoSmithKline, Stevenage, UK*
[d]*Department of Neuroscience, Janssen Pharmaceutica NV, Beerse, Belgium*

Accepted 6 October 2016

Abstract. We aimed to monitor the timing of amyloid-β deposition in relation to changes in brain function using *in vivo* imaging with [^{18}F]-AV45 and [^{18}F]-FDG in a mouse model of Alzheimer's disease. TASTPM transgenic mice and wild-type controls were scanned longitudinally with [^{18}F]-AV45 and [^{18}F]-FDG before (3 months of age) and at multiple time points after the onset of amyloid deposition (6, 9, 12, and 15 months of age). As expected with increasing amyloidosis, TASTPM mice demonstrated progressive age-dependent increases in [^{18}F]-AV45 uptake that were significantly higher than for WT from 9 months onwards and correlated to *ex vivo* measures of amyloid burden. The metabolism of [^{18}F]-AV45 produces several brain penetrant radiometabolites and normalization to a reference region helps to negate this non-specific binding and improve the sensitivity of [^{18}F]-AV45. The observed trajectory of [^{18}F]-FDG alterations deviated from our proposed hypothesis of gradual decreases with worsening amyloidosis. While [^{18}F]-FDG uptake in TASTPM mice was significantly lower than that of WT at 9 months, reduced [^{18}F]-FDG was not associated with aging in TASTPM mice. Moreover, [^{18}F]-FDG uptake did not correlate to measures of *ex vivo* amyloid burden. Our findings suggest that while amyloid-β is sufficient to induce hypometabolism, these pathologies are not linked in a dose-dependent manner in TASTPM mice.

Keywords: Alzheimer's disease, [^{18}F]-AV45, [^{18}F]-FDG, longitudinal, small animal imaging, transgenic mice

INTRODUCTION

Positron emission tomography (PET) imaging has revolutionized the ability to provide a premortem assessment of the regional and sequential pathological changes concomitant with Alzheimer's disease (AD) [1]. The combination of disease-specific amyloid positron emission tomography (PET) tracers with the neurodegenerative PET biomarker [^{18}F]-fludeoxyglucose (FDG) allows non-invasive monitoring of the extent of AD pathology and its consequent effect on brain function [2, 3]. The presence or absence of these biomarkers assists diagnosis and disease staging [4], and they are increasingly being used as inclusion criteria and secondary end points in clinical trials [5].

Transgenic mouse models that overexpress APP and PS1 mutations produce high levels of amyloid-β and are used to investigate AD pathology in a reductionist manner [6]. With the availability of small animal PET scanners, μPET imaging represents an ideal cross-species tool that enables measurement of the same molecular processes in humans and animal models. Application of amyloid tracers and [^{18}F]-FDG imaging in mouse models could then aid in basic understanding of amyloid-related neurodegeneration and additionally serve as read-outs of therapeutic efficacy of novel therapeutics.

*Correspondence to: Steven Staelens, Molecular Imaging Center Antwerp, University of Antwerp, Campus Drie Eiken – UC, Universiteitsplein 1, 2610 Wilrijk, Belgium. Tel.: +32 3 265 2820; Fax: +32 3 265 2813; E-mail: steven.staelens@uantwerpen.be.

ISSN 1387-2877/17/$35.00

With this prospect of improving translation from basic to clinical research, μPET imaging has become a thriving field in AD. Notwithstanding some initial negative findings [7–9], amyloid imaging has been successfully back-translated in a number of mouse models [10–13]. Similar to the clinical situation, research has now moved from validating to improving this technology. We, and others, have previously described discrepancies between *in vivo* uptake of amyloid tracers and gold standard *ex vivo* autoradiography [10, 11] and histology [14–16] hypothesized to derive from two main factors. The first relates to partial volume and spill over effects (PVE). While μPET systems have superior resolution to their clinical counterparts, it is insufficient in relation to the small size of mouse brain structures resulting in difficulties with accurate radioactivity measurements [17]. A second and related issue is that of high non-specific white matter uptake of amyloid tracers [18], especially in the case of [^{18}F]-florbetaben and [^{18}F]-AV45 whose metabolism is known to result in brain penetrant radiometabolites [19, 20]. Methods to counteract these effects are required so that preclinical amyloid imaging can sensitively monitor changes in amyloid burden in relation to disease progression and therapeutic response.

While small animal amyloid imaging has made considerable progression, the utility of [^{18}F]-FDG as a preclinical biomarker is disputed. Although the clinical phenotype of decreased [^{18}F]-FDG uptake has been reported in mouse models of AD [15, 16, 21, 22], an equal proportion of studies have reported increased [^{18}F]-FDG uptake [23–26]. Association studies of amyloid and hypometabolism in patients are complicated by the heterogenity of [^{18}F]-FDG uptake, which is influenced by factors such as age, genetics, comorbidities, and education levels. In this context, animal models have a clear advantage in terms of standardization of genetic and environmental backgrounds. Moreover, a number of therapies that reduced amyloid failed to demonstrate a benefit on cognition [27, 28]. Thus while amyloid imaging can provide a measure of target engagement for anti-amyloid treatments, [^{18}F]-FDG would provide insight into preservation of brain function, a more meaningful correlate to cognitive improvement.

To better formulate the strengths and limitations of amyloid tracers and [^{18}F]-FDG as translational biomarkers, we herein conducted a longitudinal μPET study in TASTPM mice. We have previously found that TASTPM mice demonstrate increased [^{18}F]-AV45 retention and decreased [^{18}F]-FDG at old age [15] and thus present a suitable model for our purposes. TASTPM mice and wild-type (WT) controls were scanned at multiple time points to cover the pathological spectrum. We hypothesized that TASTPM mice would demonstrate an age-related increase in [^{18}F]-AV45 uptake and progressive decreases in [^{18}F]-FDG uptake due to worsening disease. In relation to [^{18}F]-AV45 we conjointly probed a number of issues related to sensitivity. These included a metabolite study to quantify the contribution of radiometabolites to brain imaging and additionally an assessment of the ability of corrections for PVE (PVEC) and reference region normalization to improve early detection of amyloid pathology.

MATERIALS AND METHODS

Animals

TASTPM mice and their WT controls (C57BL/6J) were received in kind from GlaxoSmithKline (Stevenage, UK) through the PharmaCog consortium. TASTPM mice express human mutant amyloid precursor protein (hAPP695swe) and presenilin-1 (M146V) under the control of the neuron specific Thy-1 promoter on a C57BL/6J background and develop insoluble amyloid-β deposition as of 4 months of age [29]. A total of 44 male mice (22 WT and 22 TASTPM) were included in the imaging experiment. Male mice were chosen due to their lower mortality rate than females. During the course of the imaging study, 5 transgenic mice died prematurely. Additionally, at every time point an $n = 3$ for each genotype were sacrificed for histology (animals chosen at random). Table 1 displays the number of animals scanned at each time point and the average weight per genotype.

The metabolite study was performed using 3-month-old male C57BL/6J mice ($n = 11$, Harlan Laboratories, The Netherlands) and a separate aged cohort of 15-month-old WT and TASTPM mice (both $n = 11$). All animal work was performed in accordance with the European Ethics Committee (decree 86/609/CEE). The study protocol was approved by the local Animal Experimental Ethical Committee of the University of Antwerp, Belgium (2012-25).

Tracer radiosynthesis

[^{18}F]-AV45 was synthesized from the tosyloxy precursor AV-105 by modification of the method described by Yao and coworkers [30] on a

Table 1
Overview of animal numbers and average weights for the longitudinal imaging study. At every time point an $n = 3$ for each genotype were sacrificed for histology

	3 M		6 M		9 M		12 M		15 M	
	WT	TG	WT	TG	WT	TG	WT	TG	WT	TG
Weight (g)	24.79	24.02	28.41	27.58	30.45	29.72	32.18	30.61	33.39	30.54
N number	22	22	19	15	16	12	13	8	10	5

FluorSynthon I synthesis module (Comecer Netherlands, The Netherlands) that was adapted for fully automated production of [^{18}F]-AV45. [^{18}F]-FDG was prepared using a cassette based GE Fastlab synthesis module (GE Healthcare, Belgium) and was diluted with 0.9 % NaCl for injection.

Metabolite analysis

A validation study confirmed that no degradation of the tracer occurred during procedural work-up (see Supplementary Material). To evaluate the *in vivo* metabolism of [^{18}F]-AV45, mice were injected via the lateral tail vein with [^{18}F]-AV45 (37 MBq in max 200 μl). The metabolite analysis was performed on a young (3-month-old) WT cohort and an aged (15-month-old) cohort of WT and TASTPM mice ($n = 11$ for each). At 5, 10, 30, and 60 min post injection (p.i.), blood was withdrawn via cardiac puncture and the brain was rapidly removed by dissection. Plasma samples (200–400 μl), obtained after centrifugation of blood at 4500 × g for 7 min, were mixed with equal amounts of ice-cold acetonitrile for deproteination. The brain was homogenized in ice-cold acetonitrile (1 ml) and both samples were subsequently centrifuged at 4000 × g for 4 min to precipitate denatured proteins. Supernatant was separated from the precipitate and both fractions were counted in a gamma counter to calculate the extraction efficiency (percent recovery of radioactivity in the acetonitrile). 100 μl of supernatant was loaded onto a pre-conditioned reverse-phase (RP)-HPLC system (Waters XBridge, 150×4.6 mm, 5 μm HPLC column + Phenomenex security guard pre-column) and eluted with acetonitrile: NaOAc 0.05M pH5.5 (50:50 v/v) buffer at a flow rate of 1 ml/min. RP-HPLC fractions were collected at 0.5 min intervals for 13 min and radioactivity measured in a gamma counter. The radioactivity due to [^{18}F]-AV45 and each radiometabolite was expressed as a percentage of the total peak areas based on radiochromatograms. All samples had an authentic internal cold standard of AV-45 (1 mg/ml) for UV cross-validation.

PET data acquisition and processing

Animals received an awake intravenous tail vein injection of either [^{18}F]-AV45 (17.39 ± 1.49 MBq) or [^{18}F]-FDG (18.5 ± 0.74 MBq) after which mice were returned to their cages for a conscious uptake period of 30 min for [^{18}F]-AV45 and 45 min for [^{18}F]-FDG. A rest period of at least 48 h was allowed between scans. For [^{18}F]-FDG measurements, animals were fasted overnight (8–12 h) [31] prior to scanning and plasma glucose levels were monitored in duplicate by a blood glucose meter (One Touch Ultra 2, Life Scan, France) immediately after tracer injection.

20 min static PET acquisitions were acquired on two Siemens Inveon PET-CT scanners (Siemens Preclinical Solution, Knoxville, TN) [32] anesthesia was induced by inhalation of isoflurane (5% for induction, and 2% for maintenance during preparation and scanning) supplemented with oxygen. The core body temperature of the animals was maintained via a temperature controlled heating pad. In the case of [^{18}F]-FDG scans, animals in which a blood glucose measure could not be obtained were excluded due to the requirement of a glucose value for normalization purposes (one WT mouse at 9 months and one TG at 6 months). All scans were carefully assessed for movement, in this case, animals were rescanned.

All PET data was reconstructed with two-dimensional ordered subset expectation maximization (OSEM2D) [33] algorithm using 4 subsets and 16 iterations following Fourier rebinning (FORE) [34]. The energy and timing window was set to 350–650 keV and 3.432 ns, respectively. The PET images were reconstructed on a 128 × 128 × 159 grid with a pixel size of 0.776 × 0.776 × 0.776 mm. Normalization, dead time, randoms, CT-based attenuation and single scatter simulation (SSS) [35] corrections were applied. A CT was acquired subsequent to all PET scans. CT imaging was done using a 220 degrees rotation with 120 rotation steps. Voltage and amperage are set to 80 keV and 500 μA, respectively. The CT images were reconstructed using the Feldkamp filtered-backprojection algorithm.

Image processing was performed in PMOD v3.3 (PMOD technologies, Switzerland). Individual PET images were spatially normalized into the space of a predefined mouse brain template [36] by matching the individual animal specific CT to the CT template through rigid and elastic transformations and applying the same transform to the PET which is by default matched to its CT via the PET/CT scanner hardware. Processed images were subsequently co-registered with a predefined mouse brain volume-of-interest (VOI) template aligned with the aforementioned Mirrione CT/MRI atlas and tracer uptake values were extracted for each delineated VOI.

VOI-based partial volume effect correction was performed using the built-in function in PMOD [37] with the Mirrione mouse brain template. PVEC was performed using a spatial resolution of 1.5 mm × 1.5 mm × 1.5 mm isotropically and spatially invariant in PET space. Therefore, the VOI template is transformed back using the non-rigid inverse transform of the previous matching for the individual CT scan to the template. A comparison of analysis methods for quantifying [^{18}F]-AV45 uptake can be found in the Supplementary Material.

[^{18}F]AV45 uptake was quantified as i) the percent injected dose (tissue uptake[kBq/cc]/injected dose[kBq] ∗ 100) and ii) additionally by cerebellar normalization. [^{18}F]-FDG uptake was quantified as glucose-corrected SUV (tissue uptake[kBq/cc] * blood glucose[mg/dl]/injected dose[kBq] ∗ body weight[g]), albeit not normalized as the cerebellum is not a reliable reference region for [^{18}F]-FDG brain μPET [38].

Immunohistochemistry

Animals were sacrificed and brain tissue was fixed, paraffin-embedded and cut into 5 μm coronal sections. Sections were de-waxed with xylene and rehydrated by submerging in a graded series of ethanol with decreasing concentrations. First sections were bleached with potassium permanganate (3 min), rinsed in water (1 min), decolorized in oxalic acid (1 min) and rinsed again (1 min). Thereafter antigen retrieval was performed at room temperature by immersion in formic acid (10 min). Endogenous peroxidase activity was quenched by rinsing in peroxidase blocking solution (DAKO S2023) (5 min). Sections were then incubated with 4G8 primary antibody (Eurogentec SIG-39200, 1/20, 000) for 30 min (2 cycles of 15 min with rinse between incubations). Following this, sections were thoroughly rinsed in wash buffer and subsequently incubated in peroxidase coupled secondary antibody (30 min) (Envision Mouse). Sections were washed in buffer and immunodetection was performed by treatment with the chromogenic 3-3 diaminobenzidine (DAB) solution. Finally sections were counterstained with hematoxylin, dehydrated by submerging in a series of ethanol, fixed in xylene, mounted, and coverslipped. For sections stained for amyloid-β, virtual images were acquired using a Mirax Digital Slide Scanner (Carl Zeiss) and image analysis was performed using the Definiens analysis software package v1.5.

Statistics

Statistical analysis was conducted in JMP pro Version 12 (SAS Institute Inc., USA) and GraphPad Prism v6 (GraphPad Software, USA). To assess quantification methods of [^{18}F]-AV45 we compared the mean difference between WT and TASTPM uptake and then calculated the percentage difference between methods as (New data – original data)/(New data + original data)/2 * 100. The "original data" refers to [^{18}F]-AV45 quantified as %ID/g and "new data" refers to PVE corrected or PVE corrected and cerebellar normalized data. For the longitudinal study, we fitted a linear mixed model to investigate the relationship between tracer uptake ([^{18}F]-FDG or [^{18}F]-AV45), age and genotype. This method was chosen as it accounts for missing data, unbalanced designs and repeated observations within the same individual. Age and genotype were entered as "fixed effects" and mouse ID was incorporated as a random intercept ("random effect") to model subject specific responses. We additionally tested for age*genotype interactions within this model. Pairwise differences in tracer uptake between genotypes at each time point were investigated using multiple unpaired *t*-tests (with Sidak-Bonferroni correction). The correlation of μPET data to *ex vivo* histology was expressed using Pearson's correlation coefficient. Assumptions for the use of parametric *t*-tests and Pearson's correlation were met. Significance levels are given to four decimal points.

RESULTS

[^{18}F]-AV45 undergoes rapid peripheral metabolism with production of several brain penetrant metabolites

Four main radiometabolite peaks were detected in both the brain and plasma eluting with retention

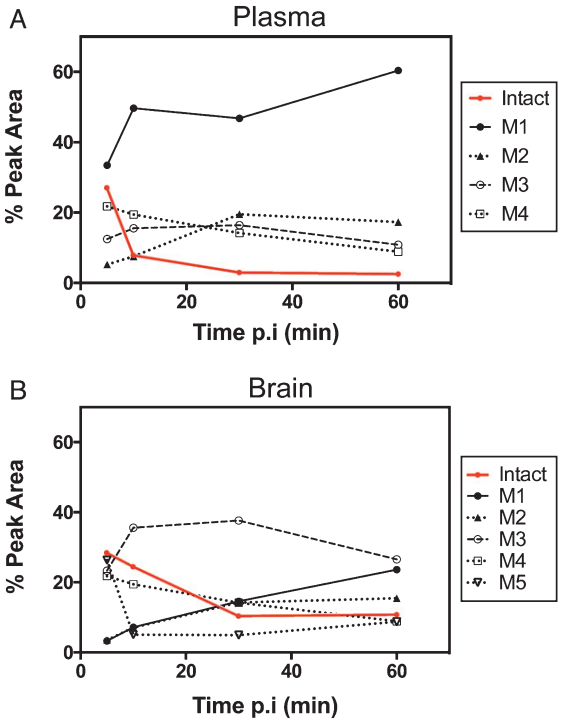

Fig. 1. [^{18}F]-AV45 is rapidly metabolized with production of several radiometabolites. Young WT mice were injected with 37 Mbq i.v of [^{18}F]AV45 and sacrificed at multiple time points p.i. The graphs show the average percentage of intact [^{18}F]-AV45 and radiometabolites in (A) the plasma and (B) the brain as a function of time. Data is presented as % peak area (mean) in the radiochromatogram. Data is presented as the mean.

times (Rt) of 1.6 min (M1), 1.85 min (M2), 3 min (M3), and 3.8 min (M4). An additional radiometabolite was observed in the brain eluting at 6.4 min (M5) very close to the intact tracer. Representative radiochromatograms for plasma and brain at 30 min p.i. are shown in Supplementary Figure 2. Figure 1A depicts the detection of [^{18}F]-AV45 and radiometabolites in plasma of healthy young WT mice. Intact [^{18}F]-AV45 accounted for $27.1 \pm 7.3\%$ of total radioactivity at 5 min p.i. decreasing rapidly to $7.9 \pm 0.73\%$ at 10 min p.i., $4.5 \pm 1.8\%$ ($n = 2$) and 5.21% ($n = 1$) at 30 and 60 min p.i., respectively. The most polar radiometabolite M1 accounted for the majority of plasma radioactivity at all time points increasing from $33.4 \pm 11.3\%$ at 5 min p.i. to $60.4 \pm 7.4\%$ at 60 min p.i.

Figure 1B illustrates the uptake of [^{18}F]-AV45 and radiometabolites in the brain of young WT mice. At 5 min p.i. levels of intact tracer in the brain were comparable to that detected in the plasma ($28.6 \pm 1.9\%$ and $27.1 \pm 7.3\%$, respectively). At all later time points, intact tracer levels were higher in the brain representing $24.6 \pm 7.6\%$, $10.6 \pm 4.3\%$, and $11.0 \pm 1.4\%$ of total radioactivity at 10, 30, and 60 min p.i., respectively. M3 was the dominant metabolite in the brain with highest levels at 10 and 30 min pi ($35.6 \pm 3.6\%$ and $37.7 \pm 3.2\%$) then declining to $26.6 \pm 1.7\%$ at 60 min p.i. The most polar metabolite M1 accumulated appreciably over time representing $23.61 \pm 2.2\%$ of total brain radioactiv-

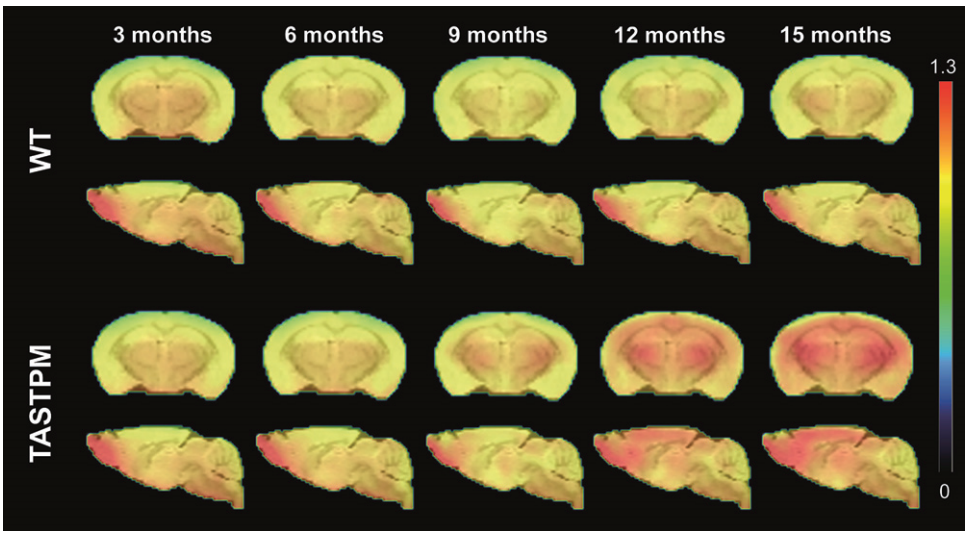

Fig. 2. Longitudinal imaging of [^{18}F]-AV45 uptake in WT and TASTPM mice. Average μPET images of [^{18}F]-AV45 uptake in WT and TASTPM mice at each time point. [^{18}F]-AV45 uptake was corrected for injected dose and normalized to the cerebellum. μPET images are overlaid on a T_2-weighted MRI template for anatomic localization. 3 months (TASTPM = 22, WT = 22), 6 months (TASTPM = 15, WT = 19), 9 months (TASTPM = 12, WT = 16), 12 months (TASTPM = 8, WT = 13), 15 months (TASTPM = 5, WT = 10).

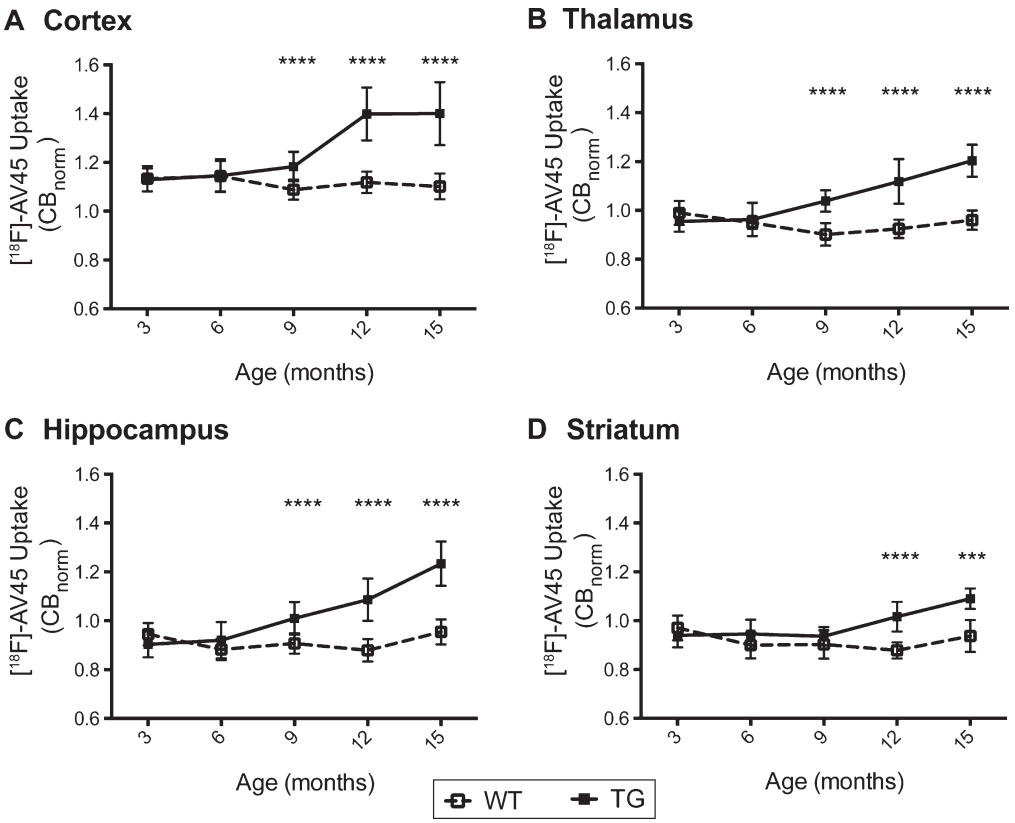

Fig. 3. TASTPM mice demonstrate age-related increases in [^{18}F]-AV45 uptake. Figures A-D show regional uptake values of [^{18}F]-AV45 in both genotypes over time. [^{18}F]-AV45 uptake in each region was presented as a ratio to the cerebellum (CBnorm). Data is shown as mean ± standard deviation. Differences between genotypes at each time point were evaluated with *t*-tests (with Sidak-Bonferroni correction), ****$p < 0.0001$, ***$p < 0.001$.

ity by 60 min p.i. (Fig. 1B). While the extraction yields from plasma remained relatively constant (85.8 ± 3.9% at 5 min p.i. to 87.2 ± 0.7% at 60 min p.i.), the extraction of radioactivity from the brain decreased as a function of time (86.1 ± 1.2% at 5 min p.i. to 65.1 ± 4.8% at 30 min p.i.). Results obtained from the aged WT and TASTPM cohorts were largely congruent with those described for young WT (Supplemental Table 2).

TASTPM mice demonstrate age-dependent increases in [^{18}F]-AV45 uptake

The uptake of [^{18}F]-AV45 averaged over the WT and TASTPM groups is visualized across time points in Fig. 2. Figure 3A-D show the time course of [^{18}F]-AV45 uptake in the cortex, thalamus, hippocampus, and striatum of WT and TASTPM mice in all animals investigated. A highly significant interaction of age*genotype was found for all regions investigated ($p < 0.0001$), supporting an age-dependent increase in [^{18}F]-AV45 uptake in TASTPM mice. Using multiple *t*-tests, we compared [^{18}F]-AV45 uptake between WT and TASTPM cross-sectionally at each time-point to test for increased [^{18}F]-AV45 uptake in TASTPM mice. TASTPM uptake was significantly higher at 9 months in the cortex ($t_{(26)} = 4.94$, $p < 0.0001$), thalamus ($t_{(26)} = 7.93$, $p < 0.0001$), and hippocampus ($t_{(26)} = 4.96$, $p < 0.0001$), in the striatum at 12 months ($t_{(19)} = 6.82$, $p < 0.0001$) and remains significantly higher at all further time points. In the TASTPM mice ($n = 5$) that underwent scanning at all time points, the average % increase from baseline was 23.7 ± 8.4% in the cortex, 28.5 ± 8.6% in the thalamus, 35.6 ± 8.8% in the hippocampus, and 19.2 ± 9.4% in the striatum.

Reductions in [^{18}F]-FDG uptake do not worsen with age in TASTPM mice

Figure 5A-D shows the average uptake of [^{18}F]-FDG in the cortex, thalamus, hippocampus, and striatum of WT and TASTPM mice in all animals

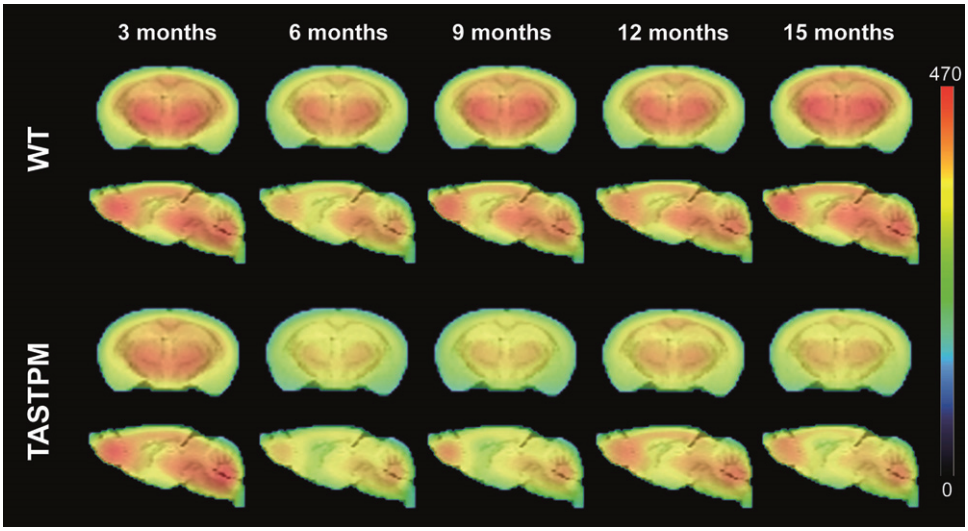

Fig. 4. Longitudinal imaging of [^{18}F]-FDG uptake in WT and TASTPM mice. Average μPET images of [^{18}F]-FDG uptake in WT and TASTPM mice at each time point. [^{18}F]-FDG uptake was corrected for injected dose, body weight and pre-scan blood glucose, (tissue uptake[kBq/cc] * blood glucose/injected dose[kBq] * body weight). μPET images are overlaid on a T_2-weighted MRI template for anatomic localization. 3 months (TASTPM = 22, WT = 22), 6 months (TASTPM = 13, WT = 19), 9 months (TASTPM = 12, WT = 14), 12 months (TASTPM = 8, WT = 13), 15 months (TASTPM = 5, WT = 10).

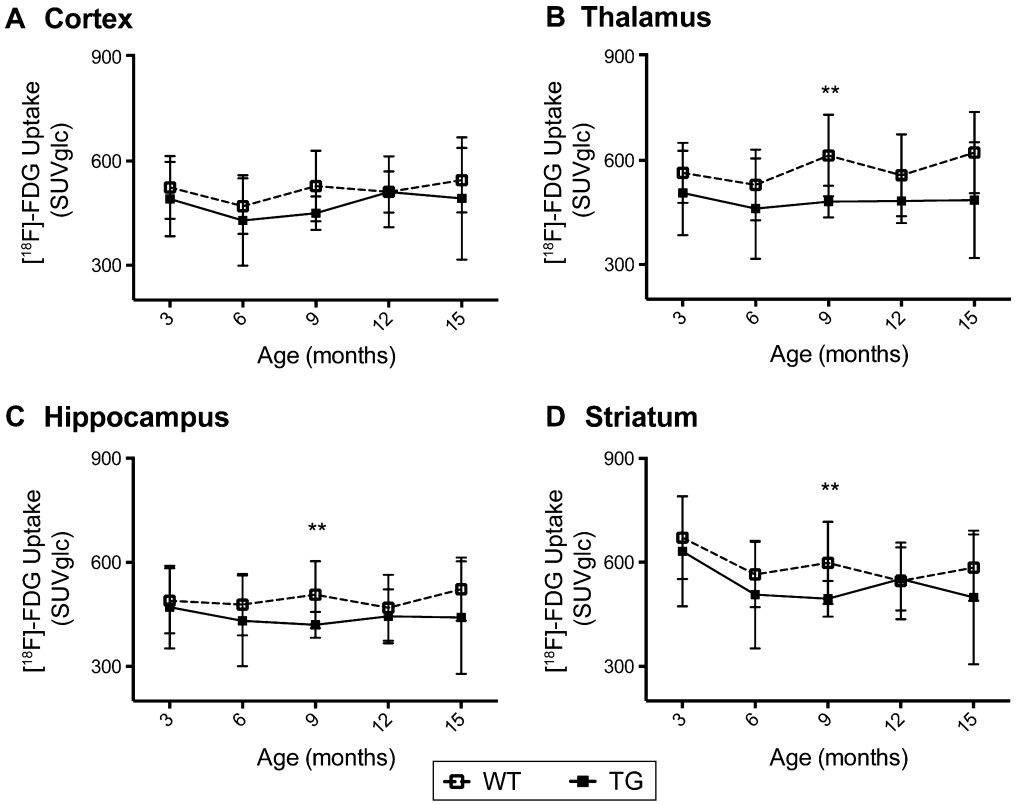

Fig. 5. TASTPM mice demonstrate lower [^{18}F]-FDG uptake in comparison to WT that does not worsen with disease progression. Panels A-D show regional uptake values of [^{18}F]-FDG in both genotypes over time. [^{18}F]-FDG uptake is quantified as glucose-corrected SUV (tissue uptake[kBq/cc] * blood glucose[mg/dl]/injected dose[kBq] * body weight[g]). Data is shown as mean ± standard deviation. Differences between genotypes at each time point were evaluated with *t*-tests (with Sidak-Bonferroni correction), $^{**}p < 0.01$.

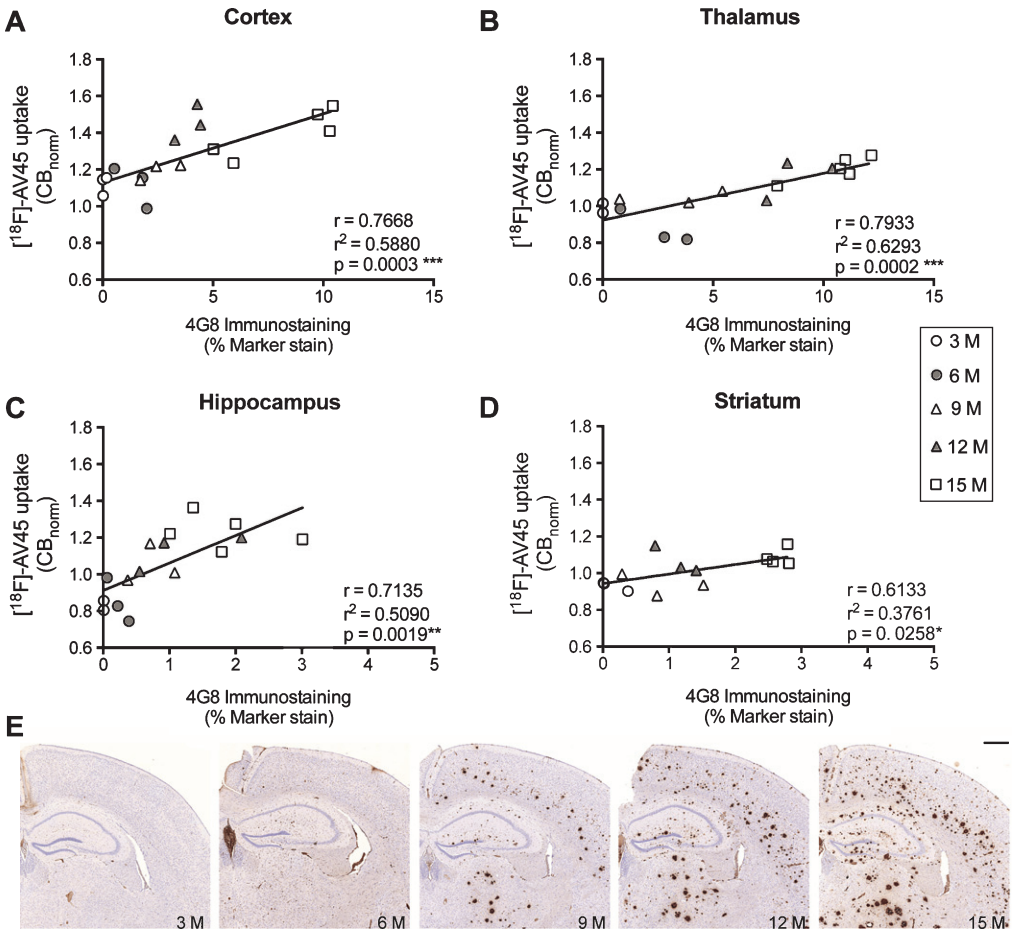

Fig. 6. Comparison of *in vivo* amyloid imaging and *ex vivo* quantification of amyloid burden. Graphs A-D show correlation analysis of regional [^{18}F]-AV45 uptake and amyloid burden detected by 4G8 immunostaining. Panel E shows representative 4G8 immunohistochemistry in TASTPM mice at each age. Scale bar = 500 μm.

investigated for each time point and are visualized in Fig. 4. No interaction of age* genotype was demonstrated, thus TASTPM mice do not show progressive age-related decreases in [^{18}F]-FDG uptake. We found a significant main effect of genotype for all regions, cortex ($p = 0.0393$), hippocampus ($p = 0.0248$), striatum ($p = 0.0365$), and thalamus ($p = 0.0004$) supporting that [^{18}F]-FDG uptake was lower in TASTPM mice. A significant main effect of age was found only in the striatum ($p = 0.0004$). Using multiple *t*-tests, we compared [^{18}F]-FDG uptake between WT and TASTPM cross-sectionally at each time-point. [^{18}F]-FDG uptake was significantly lower at 9 months in the thalamus ($t_{(24)} = 3.69$, $p = 0.0012$), hippocampus ($t_{(24)} = 2.92$, $p = 0.0075$), and striatum ($t_{(24)} = 2.81$, $p = 0.0097$). At 12 months, [^{18}F]-FDG uptake is similar to that of WT in the cortex, hippocampus, and striatum.

In vivo uptake of [^{18}F]-AV45, but not [^{18}F]-FDG, correlates with ex vivo measures of amyloid-β

Figure 6A-D depict correlation analysis between *ex vivo* 4G8 immunostaining and *in vivo* tracer uptake in TASTPM mice by region for all time points. All regions demonstrated significant positive correlations between [^{18}F]-AV45 uptake and histology. The strongest relationship was found in the thalamus ($r = 0.7933$, $p = 0.0002$), followed by the cortex ($r = 0.7668$, $p = 0.0003$), hippocampus ($r = 0.7135$, $p = 0.0019$), and striatum ($r = 0.6133$, $p = 0.0258$). A high amount of non-specific staining was observed in the striatum at 6 months of age, no plaques were present, and the data were not included in the correlation analysis. No relationship between [^{18}F]-FDG and *ex vivo* measures of amyloid-β burden was demonstrated (data not shown). Figure 6E shows

representative images from immunostained brain slices of TASTPM mice at each age. Plaque pathology was absent in the cerebellum of TASTPM mice (Supplementary Figure 3) and in the brains of WT mice.

DISCUSSION

Translation of basic research findings into clinical drug development depends largely on animal models as a means to uncover pathomechanisms and to predict therapeutic efficacy. A lack of appropriate biomarkers that transfer from animal models to human is widely acknowledged as a rate-limiting step in translational research [39]. μPET imaging is particularly attractive for animal model-based research and represents a translational tool that would allow for greater conformity between human and animal studies. We herein investigated the potential of [^{18}F]-AV45 and [^{18}F]-FDG as translational biomarkers in double transgenic TASTPM mice.

[^{18}F]-AV45 is gaining wide application in clinical and preclinical research as a non-invasive marker of disease progression. Excellent brain penetrance, rapid washout kinetics and a high affinity against amyloid-β are among the qualities that recommend [^{18}F]-AV45 as a suitable imaging agent [20, 40]. Being fluorinated, it has the added benefits of increased availability in comparison to its predecessor, [^{11}C]-PiB. However, one disadvantage of [^{18}F]-AV45 is its notably lower dynamic range due to high non-specific white matter binding [41], which we have previously shown to result in smaller differences between WT and transgenic mice [16]. Herein, as part of our investigations into the sensitivity of [^{18}F]-AV45, we aimed to assess the production and brain uptake of radiometabolites. While fast metabolism and brain penetrant radiometabolites of [^{18}F]-AV45 have been reported [20], we believe that both the extent of plasma clearance and contribution of radiometabolites to brain imaging has been underestimated. In contrast to a previous report of a plasma half-life of <30 min [20], we herein found a half-life of <5 min. The contribution of radiometabolites to brain imaging is substantial with radiometabolites comprising 70% of brain radioactivity already at 5–10 min. Moreover, these radiometabolites bind and are retained in the brain as shown by the decreasing extraction efficiency from brain tissue (from 86.1% at 5 min p.i. to 65.1% at 30 min p.i.). This high amount of non-specific binding dilutes signal specificity thus limiting the sensitivity of [^{18}F]-AV45. The use of PVEC and cerebellar normalized data produced the expected progressive increases in [^{18}F]-AV45 uptake in TASTPM and this *in vivo* uptake correlated strongly to histology. Overall, the age-dependent increases in [^{18}F]-AV45 uptake are in agreement with the growing body of data supporting amyloid imaging in mouse models.

The utility of [^{18}F]-FDG as a translational biomarker is more complicated. While the significant main effect of genotype supports a pathological reduction of [^{18}F]-FDG uptake in TASTPM mice, the lack of an interaction with age implies that hypometabolism is not associated with aging, and by extension, also not with worsening pathology. This presents clear differences to the human situation. In previous studies, lack of [^{18}F]-FDG reductions in mouse models of AD were hypothesized to arise from glial uptake of [^{18}F]-FDG in response to increased energetic demands during neuroinflammation. Age-dependent increases in activated glial cells have been reported in TASTPM mice [42, 43] and thus such a mechanism could account for the absence of age-related decreases in [^{18}F]-FDG uptake. However, in our previous study of TASTPM mice at 13.5 months, we detected significant reductions in [^{18}F]-FDG uptake despite immunohistochemistry demonstrating an increased number of microglia and astrocytes [15]. In this former study, we found the thalamus to demonstrate the most pronounced reductions in [^{18}F]-FDG and herein the thalamus also demonstrated the greatest reductions in [^{18}F]-FDG uptake, albeit at 9 M. The reduced statistical power at 12 and 15 months due to the lower sample size may have limited the ability to determine changes in [^{18}F]-FDG uptake at these ages and could account for differences to our findings in 13.5 month TASTPM mice.

Amyloidosis models do not recapitulate the entire disease spectrum of AD and are devoid of tau tangle pathology and overt neuronal loss [44]. The absence of these pathological hallmarks likely underlies the inability of [^{18}F]-FDG imaging to wholly mimic clinical observations. Although fewer investigations of [^{18}F]-FDG have been performed in tau transgenic models, these studies have demonstrated decreasing [^{18}F]-FDG uptake in relation to increasing tau pathology with age [45] (Deleye et al., unpublished data). Moreover, while we have found no correlation between [^{18}F]-FDG decreases and amyloid-β pathology in amyloidosis models, a relationship between tau pathology and hypometabolism has been demonstrated in these tauopathy models [45]

(Deleye et al., unpublished data). The present results suggest a complex relationship between amyloid-β and hypometabolism. Further information on the connection between amyloid-β and hypometabolism could be gleaned from manipulating amyloid levels, for instance by a treatment, to investigate the resultant effect on brain metabolism. Such an investigation would furthermore serve as a continued evaluation of the utility of [^{18}F]-FDG as a preclinical biomarker.

ACKNOWLEDGMENTS

This work was funded by Antwerp University and its University Hospital, Antwerp, Belgium through an assistant professor position for L.w. and J.V; an associate professor position for St.S and a full professor position for Si. St. AMW is supported through an IWT scholarship (Agency for Innovation by Science and Technology). XL and MS are with Janssen Pharmaceutica, Beerse, Belgium holding a contract research program with the Molecular Imaging Center Antwerp. JR is with GSK. The authors are thankful to Philippe Joye (Molecular Imaging Center Antwerp) for support with *in vivo* experiments. We would also like to thank Dr. José Ignacio Andrés (Janssen Research and Development, Toledo, Spain) for preparation of AV-105 and cold reference and Dr. An Torremans and Hilde Vermeirsch from Histogenex for *ex vivo* validation processing. The authors are additionally thankful to Erik Franssen for statistical assistance. This research was performed in conjunction with the European Community's Seventh Framework Program (FP7/2007-2013) for the Innovative Medicine Initiative under the PharmaCog Grant Agreement n°115009.

Authors' disclosures available online (http://j-alz.com/manuscript-disclosures/16-0760r1).

SUPPLEMENTARY MATERIAL

The supplementary material is available in the electronic version of this article: http://dx.doi.org/10.3233/JAD-160760.

REFERENCES

[1] Barthel H, Seibyl J, Sabri O (2015) The role of positron emission tomography imaging in understanding Alzheimer'sdisease. *Expert Rev Neurother* **15**, 395-406.

[2] Mosconi L, Berti V, Glodzik L, Pupi A, De Santi S, De Leon MJ (2009) Pre-clinical detection of Alzheimer's disease using FDG-PET, with or without amyloid imaging. *J Alzheimers Dis* **20**, 843-854.

[3] Mosconi L, McHugh PF (2011) FDG- and amyloid-PET in Alzheimer's disease: Is the whole greater than the sum of the parts? *Q J Nucl Med Mol Imaging* **55**, 250-264.

[4] Mormino EC, Betensky RA, Hedden T, Schultz AP, Amariglio RE, Rentz DM, Johnson KA, Sperling RA (2014) Synergistic effect of β-amyloid and neurodegeneration on cognitive decline in clinically normal individuals. *JAMA Neurol* **71**, 1379.

[5] Mattsson N, Carrillo MC, Dean RA, Devous MD Sr, Nikolcheva T, Pesini P, Salter H, Potter WZ, Sperling RS, Bateman RJ, Bain LJ, Liu E (2015) Revolutionizing Alzheimer's disease and clinical trials through biomarkers. *Alzheimers Dement (Amst)* **1**, 412-419.

[6] Götz J, Ittner LM (2008) Animal models of Alzheimer's disease and frontotemporal dementia. *Nat Rev Neurosci* **9**, 532-544.

[7] Kuntner C, Kesner AL, Bauer M, Kremslehner R, Wanek T, Mandler M, Karch R, Stanek J, Wolf T, Müller M, Langer O (2009) Limitations of small animal PET imaging with [18F]FDDNP and FDG for quantitative studies in a transgenic mouse model of Alzheimer's disease. *Mol Imaging Biol* **11**, 236-240.

[8] Toyama H, Ye D, Ichise M, Liow J-S, Cai L, Jacobowitz D, Musachio JL, Hong J, Crescenzo M, Tipre D, Lu J-Q, Zoghbi S, Vines DC, Seidel J, Katada K, Green MV, Pike VW, Cohen RM, Innis RB (2005) PET imaging of brain with the beta-amyloid probe, [11C]6-OH-BTA-1, in a transgenic mouse model of Alzheimer's disease. *Eur J Nucl Med Mol Imaging* **32**, 593-600.

[9] Klunk WE, Lopresti BJ, Ikonomovic MD, Lefterov IM, Koldamova RP, Abrahamson EE, Debnath ML, Holt DP, Huang G-F, Shao L, DeKosky ST, Price JC, Mathis CA (2005) Binding of the positron emission tomography tracer Pittsburgh compound-B reflects the amount of amyloid-beta in Alzheimer's disease brain but not in transgenic mouse brain. *J Neurosci* **25**, 10598-10606.

[10] Poisnel G, Dhilly M, Moustié O, Delamare J, Abbas A, Guilloteau D, Barré L (2012) PET imaging with [18F]AV-45 in an APP/PS1-21 murine model of amyloid plaque deposition. *Neurobiol Aging* **33**, 2561-2571.

[11] Rominger A, Brendel M, Burgold S, Keppler K, Baumann K, Xiong G, Mille E, Gildehaus FJ, Carlsen J, Schlichtiger J, Niedermoser S, Wängler B, Cumming P, Steiner H, Herms J, Haass C, Bartenstein P (2013) Longitudinal assessment of cerebral β-amyloid deposition in mice overexpressing Swedish mutant β-amyloid precursor protein using 18F-florbetaben PET. *J Nucl Med* **54**, 1127-1134.

[12] Snellman A, Lopez-Picon FR, Rokka J, Salmona M, Forloni G, Scheinin M, Solin O, Rinne JO, Haaparanta-Solin M (2013) Longitudinal amyloid imaging in mouse brain with 11C-PIB: Comparison of APP23, Tg2576, and APPswePS1dE9 mouse models of Alzheimer disease. *J Nucl Med* **54**, 1434-1441.

[13] Sérrière S, Tauber C, Vercouillie J, Mothes C, Pruckner C, Guilloteau D, Kassiou M, Doméné A, Garreau L, Page G, Chalon S (2015) Amyloid load and translocator protein 18 kDa in APPswePS1-dE9 mice: A longitudinal study. *Neurobiol Aging* **36**, 1639-1652.

[14] Waldron A-M, Verhaeghe J, wyffels L, Schmidt M, Langlois X, Van der Linden A, Stroobants S, Staelens S (2015) Preclinical comparison of the amyloid-β radioligands [(11)C]Pittsburgh compound B and [(18)F]florbetaben in

aged APPPS1-21 and BRI1-42 mouse models of cerebral amyloidosis. *Mol Imaging Biol* **17**, 688-696.

[15] Waldron A, Wyffels L, Verhaeghe J, Bottelbergs A, Richardson J, Kelley J, Schmidt M, Stroobants S, Langlois X, Staelens S (2015) Quantitative muPET imaging of cerebral glucose metabolism and amyloidosis in the TASTPM double transgenic mouse model of Alzheimer's disease. *Curr Alzheimer Res* **12**, 694-703.

[16] Waldron A-M, Wintmolders C, Bottelbergs A, Kelley JB, Schmidt ME, Stroobants S, Langlois X, Staelens S (2015) In vivo molecular neuroimaging of glucose utilization and its association with fibrillar amyloid-β load in aged APPPS1-21 mice. *Alzheimers Res Ther* **7**, 76.

[17] Lehnert W, Gregoire M-C, Reilhac A, Meikle SR (2012) Characterisation of partial volume effect and region-based correction in small animal positron emission tomography (PET) of the rat brain. *Neuroimage* **60**, 2144-2157.

[18] Fodero-Tavoletti MT, Rowe CC, McLean CA, Leone L, Li Q-X, Masters CL, Cappai R, Villemagne VL (2009) Characterization of PiB binding to white matter in Alzheimer disease and other dementias. *J Nucl Med* **50**, 198-204.

[19] Patt M, Schildan A, Barthel H, Becker G, Schultze-Mosgau MH, Rohde B, Reininger C, Sabri O (2010) Metabolite analysis of [18F]Florbetaben (BAY 94-9172) in human subjects: A substudy within a proof of mechanism clinical trial. *J Radioanal Nucl Chem* **284**, 557-562.

[20] Choi SR, Golding G, Zhuang Z, Zhang W, Lim N, Hefti F, Benedum TE, Kilbourn MR, Skovronsky D, Kung HF (2009) Preclinical properties of 18F-AV-45: A PET agent for Abeta plaques in the brain. *J Nucl Med* **50**, 1887-1894.

[21] Platt B, Drever B, Koss D, Stoppelkamp S, Jyoti A, Plano A, Utan A, Merrick G, Ryan D, Melis V, Wan H, Mingarelli M, Porcu E, Scrocchi L, Welch A, Riedel G (2011) Abnormal cognition, sleep, EEG and brain metabolism in a novel knock-in Alzheimer mouse, PLB1. *PLoS One* **6**, e27068.

[22] Macdonald IR, Debay DR, Reid GA, O'Leary TP, Jollymore CT, Mawko G, Burrell S, Martin E, Bowen CV, Brown RE, Darvesh S (2014) Early detection of cerebral glucose uptake changes in the 5XFAD mouse. *Curr Alzheimer Res* **11**, 450-460.

[23] Brendel M, Probst F, Jaworska A, Overhoff F, Korzhova V, Albert N, Beck R, Lindner S, Gildehaus FJ, Baumann K, Bartenstein P, Kleinberger G, Haass C, Herms J, Rominger A (2016) Glial activation and glucose metabolism in a transgenic amyloid mouse model: A triple tracer PET study. *J Nucl Med* **57**, 954-960.

[24] Poisnel G, Hérard A-S, Tannir El Tayara El N, Bourrin E, Volk A, Kober F, Delatour B, Delzescaux T, Debeir T, Rooney T, Benavides J, Hantraye P, Dhenain M (2012) Increased regional cerebral glucose uptake in an APP/PS1 model of Alzheimer's disease. *Neurobiol Aging* **33**, 1995-2005.

[25] Luo F, Rustay NR, Ebert U, Hradil VP, Cole TB, Llano DA, Mudd SR, Zhang Y, Fox GB, Day M (2012) Characterization of 7- and 19-month-old Tg2576 mice using multimodal in vivo imaging: Limitations as a translatable model of Alzheimer's disease. *Neurobiol Aging* **33**, 933-944.

[26] Rojas S, Herance JR, Gispert JD, Abad S, Torrent É, Jiménez X, Pareto D, Perpiña U, Sarroca S, Rodríguez E, Ortega-Aznar A, Sanfeliu C (2013) In vivo evaluation of amyloid deposition and brain glucose metabolism of 5XFAD mice using positron emission tomography. *Neurobiol Aging* **34**, 1790-1798.

[27] Salloway S, Sperling R, Fox NC, Blennow K, Klunk W, Raskind M, Sabbagh M, Honig LS, Porsteinsson AP, Ferris S, Reichert M, Ketter N, Nejadnik B, Guenzler V, Miloslavsky M, Wang D, Lu Y, Lull J, Tudor IC, Liu E, Grundman M, Yuen E, Black R, Brashear HR (2014) Two Phase 3 trials of bapineuzumab in mild-to-moderate Alzheimer's disease. *N Engl J Med* **370**, 322-333.

[28] Lobello K, Ryan JM, Liu E, Rippon G, Black R (2012) Targeting beta amyloid: A clinical review of immunotherapeutic approaches in Alzheimer's disease. *Int J Alzheimers Dis* **2012**, 1-14.

[29] Howlett DR, Richardson JC, Austin A, Parsons AA, Bate ST, Davies DC, Gonzalez MI (2004) Cognitive correlates of Abeta deposition in male and female mice bearing amyloid precursor protein and presenilin-1 mutant transgenes. *Brain Res* **1017**, 130-136.

[30] Yao C-H, Lin W-L, Weng C-C, Hsiao I-T, Ting Y-S, Yen T-C, Jan T-R, Skovronsky D, Kung M-P, Wey S-P (2010) GMP-compliant automated synthesis of [(18)F]AV-45 (Florbetapir F 18) for imaging beta-amyloid plaques in human brain. *Appl Radiat Isot* **68**, 2293-2297.

[31] Wong KP, Sha W, Zhang X, Huang SC (2011) Effects of Administration route, dietary condition, and blood glucose level on kinetics and uptake of 18F-FDG in mice. *J Nucl Med* **52**, 800-807.

[32] Kemp BJ, Hruska CB, McFarland AR, Lenox MW, Lowe VJ (2009) NEMA NU 2-2007 performance measurements of the Siemens Inveon preclinical small animal PET system. *Phys Med Biol* **54**, 2359-2376.

[33] Hudson HM, Larkin RS (1993) Accelerated image reconstruction using ordered subsets of projection data. *IEEE Trans Med Imaging* **13**, 601-609.

[34] Defrise M, Kinahan PE, Townsend DW, Michel C, Sibomana M, Newport DF (1997) Exact and approximate rebinning algorithms for 3-D PET data. *IEEE Trans Med Imaging* **16**, 145-158.

[35] Watson CC (2000) New, faster, image-based scatter correction for 3D PET. *IEEE Trans Nucl Sci* **47**, 1587-1594.

[36] Mirrione MM, Schiffer WK, Fowler JS, Alexoff DL, Dewey SL, Tsirka SE (2007) A novel approach for imaging brain-behavior relationships in mice reveals unexpected metabolic patterns during seizures in the absence of tissue plasminogen activator. *Neuroimage* **38**, 34-42.

[37] Rousset OG, Ma YL, Evans AC (1998) Correction for partial volume effects in PET: Principle and validation. *J Nucl Med* **39**, 904-911.

[38] Deleye S, Waldron A-M, Richardson JC, Schmidt M, Langlois X, Stroobants S, Staelens S (2016) The effects of physiological and methodological determinants on 18F-FDG mouse brain imaging exemplified in a double transgenic Alzheimer model. *Mol Imaging* **15**, doi: 10.1177/1536012115624919.

[39] Shineman DW, Basi GS, Bizon JL, Colton CA, Greenberg BD, Hollister BA, Lincecum J, Leblanc GG, Lee LBH, Luo F, Morgan D, Morse I, Refolo LM, Riddell DR, Scearce-Levie K, Sweeney P, Yrjänheikki J, Fillit HM (2010) Accelerating drug discovery for Alzheimer's disease: Best practices for preclinical animal studies. *Alzheimers Res Ther* **3**, 28.

[40] Clark CM, Pontecorvo MJ, Beach TG, Bedell BJ, Coleman RE, Doraiswamy PM, Fleisher AS, Reiman EM, Sabbagh MN, Sadowsky CH, Schneider JA, Arora A, Carpenter AP, Flitter ML, Joshi AD, Krautkramer MJ, Lu M, Mintun MA, Skovronsky DM (2012) Cerebral PET with florbetapir compared with neuropathology at autopsy for detection of neuritic amyloid-β plaques: A prospective cohort study. *Lancet Neurol* **11**, 669-678.

[41] Landau SM, Thomas BA, Thurfjell L, Schmidt M, Margolin R, Mintun M, Pontecorvo M, Baker SL, Jagust WJ, Alzheimer's Disease Neuroimaging Initiative (2014) Amyloid PET imaging in Alzheimer's disease: A comparison of three radiotracers. *Eur J Nucl Med Mol Imaging* **41**, 1398-1407.

[42] Howlett DR, Bowler K, Soden PE, Riddell D, Davis JB, richardson JC, Burbidge SA, Gonzalez MI, Irving EA, Lawman A, Miglio G, Dawson EL, Howlett ER, Hussain I (2008) Abeta deposition and related pathology in an APP x PS1 transgenic mouse model of Alzheimer's disease. *Histol Histopathol* **23**, 67-76.

[43] Roberts JC, Friel SL, Roman S, Perren M, Hardy J, Davis JB, Richardson JC, Virley D, Medhurst AD (2009) Autoradiographical imaging of PPARγ agonist effects on PBR/TSPO binding in TASTPM mice. *Exp Neurol* **216**, 459-470.

[44] LaFerla FM, Green KN (2012) Animal models of Alzheimer disease. *Cold Spring Harb Perspect Med* **2**, a006320.

[45] de Cristóbal J, García-García L, Delgado M, Pérez M, Pozo MA, Medina M (2014) Longitudinal assessment of a transgenic animal model of tauopathy by FDG-PET imaging. *J Alzheimers Dis* **40**(Suppl 1), S79-S89.